



LAWRENCE
LIVERMORE
NATIONAL
LABORATORY

Driving toroidally asymmetric current through the tokamak scrape-off layer, Part II: Magnetic field structure and spectrum

I. Joseph

April 10, 2009

Physics of Plasmas

Disclaimer

This document was prepared as an account of work sponsored by an agency of the United States government. Neither the United States government nor Lawrence Livermore National Security, LLC, nor any of their employees makes any warranty, expressed or implied, or assumes any legal liability or responsibility for the accuracy, completeness, or usefulness of any information, apparatus, product, or process disclosed, or represents that its use would not infringe privately owned rights. Reference herein to any specific commercial product, process, or service by trade name, trademark, manufacturer, or otherwise does not necessarily constitute or imply its endorsement, recommendation, or favoring by the United States government or Lawrence Livermore National Security, LLC. The views and opinions of authors expressed herein do not necessarily state or reflect those of the United States government or Lawrence Livermore National Security, LLC, and shall not be used for advertising or product endorsement purposes.

Driving toroidally asymmetric current through the tokamak scrape-off layer,

Part II: Magnetic field structure and spectrum

Ilon Joseph*

Lawrence Livermore National Laboratory

(Dated: April 8, 2009)

Abstract

The structure of the magnetic field perturbations due to non-axisymmetric field-aligned currents in the tokamak scrape-off layer (SOL) are analytically calculated near the X-point. Part I [I. Joseph, et al., submitted to Phys. Plasmas (2008)] demonstrated that biasing divertor target plates in a toroidally asymmetric fashion can generate an appreciable toroidally asymmetric parallel current density in the SOL along the separatrix. Here, the magnetic field perturbation caused by a SOL current channel of finite width and step-wise constant amplitude at the target plate is derived. Flux expansion amplifies the magnetic perturbation near the X-point, while phase interference causes the SOL amplitude to be reduced at large toroidal mode number. Far enough from the current channel, the magnetic field can be approximated as arising from a surface current near the separatrix with differing amplitudes in the SOL and the divertor leg. The perturbation spectrum and resonant components of this field are computed analytically asymptotically close to the separatrix in magnetic flux coordinates. The size of the stochastic layer due to the applied perturbation that would result without self-consistent plasma shielding is also estimated. If enough resonant field is generated, control of the edge pressure gradient may allow stabilization of edge localized modes.

PACS numbers: 28.52.-s, 28.52.Av, 52.55.Fa, 52.55.Rk

Keywords: Fusion reactors, tokamaks, spherical tokamaks, power exhaust, divertors

*joseph5@llnl.gov

I. INTRODUCTION

Driving toroidally asymmetric current through the scrape-off layer (SOL) of a diverted tokamak has been proposed [1–4] as a potentially useful tool for mitigating the large heat fluxes that are delivered to the divertor target plates of a fusion reactor [5–7]. Toroidally asymmetric electrostatic fields were originally proposed to create convection cells in the divertor to spread turbulent heat flux [1–3]. Ref. [4] proposes driving asymmetric SOL current to suppress edge localized modes (ELMs) which rapidly deliver unacceptable levels of impulsive heat flux during high-performance operation [6–8]. SOL currents are also known to be internally generated by magnetohydrodynamic (MHD) instabilities such as ELMs and tearing modes and have been measured in Refs. [9–12]. Important questions arise for understanding the magnetic effects of the toroidally asymmetric SOL current: What is the spatial structure of the driven magnetic perturbation? What is the spectral structure of the perturbation field in magnetic coordinates? Are the spectral components sufficiently large to drive a region of magnetic stochasticity or enhance edge neoclassical transport? In this article, steps toward answering these questions are taken by analytically describing the spatial and spectral structure of magnetic field perturbations generated by the SOL current.

The stability of large (Type-I) ELMs is highly sensitive to the structure of both the parallel current and pressure gradient instability drives at the edge of an H-mode tokamak [13, 14]. Reduction of the pressure gradient can be achieved by breaking the toroidal symmetry of the magnetic field in order to enhance transport. The technique of applying resonant magnetic perturbations (RMP) to the tokamak edge has been shown to significantly impact H-mode particle balance [15–19], causing the plasma density and the edge pressure gradient to be reduced to a level below the ELM stability limit [17, 18]. Experimentally, the critical requirement is that, relative to the main toroidal field B_t , the flux surface averaged Fourier component of the perturbation field that resonates with the pitch of the field lines at the plasma edge must satisfy $\tilde{B}_{mn} > 10^{-4} B_t$. For the pitch resonant component, $m = qn$ where q is the safety factor and m/n are the poloidal/toroidal mode numbers. The first hypothesis was that magnetic field line stochasticity could explain the results [15, 16] and this has been taken as guide for recent the design studies [20, 21]. However, this appears inconsistent with the lack of an observable enhancement to thermal conduction [18, 22, 23] and is in conflict with the intrinsic tearing stability of the rotating plasma [24–26]. Enhanced neo-

classical transport may dominate when self-consistent plasma response effects are correctly accounted for [27–29].

This article is the second part of a series of two articles analyzing the possibility that asymmetric SOL currents can be used to control ELMs. In Part I, a qualitative upper limit for the RMP amplitude was determined from the total amount of parallel current that can be driven across the target plate. Because the current density is assumed to travel within a relatively thin layer near the plasma surface, an estimate of the total surface current density across the layer leads to a useful estimate for the characteristic magnetic field that can be generated. For observation points that are closer to the current channel than the toroidal or poloidal wavelength, the field produced by the surface current K can still be estimated from the discontinuity in the tangential field $[B] = 4\pi K/c$, where c represents the speed of light. If the target is biased to potentials of order the electron temperature, the current density that can be driven will be limited by the ion saturation current density J_{sat} . The width of the parallel particle flux at the target plate Δr gives an upper limit for the maximum surface current density that can be drawn $K_{sat} = J_{sat}\Delta r$. The corresponding magnetic field perturbation amplitude near the target plate is then $\tilde{B}_{sat} = [B]/2 = 2\pi K_{sat}/c$. Part I estimated that for ITER the total parallel ion saturation current across the target $10^2 - 10^3$ A/cm is large enough to produce characteristic fields of $10^2 - 10^3$ G. Such fields exceed the RMP threshold by factors of 10 – 100.

Part I also developed a more quantitative analysis of the spatial structure of the current density. Flux expansion causes the surface current to become large near the X-point. However, the shearing of field lines as they pass the X-point causes the coherent perturbation to be reduced in the SOL. Radially across the divertor leg the current density is in phase, but radially across the SOL rapid oscillations due to phase shearing near the separatrix reduce the amplitude of the net surface current. The efficiency of the SOL current drive ε_{sol} was measured by the ratio between the net SOL surface current density to the maximum density possible, given the maximum value at the target K_{sat} and the intrinsic dependence on flux expansion. The efficiency is sensitive to toroidal mode number n and the geometry of the divertor and the phasing of the biased target plate. At low n , a useful range of efficiencies can be achieved by optimizing the biasing geometry.

A more accurate estimate for the average field in the SOL is given by

$$\tilde{B}_{sol} = \varepsilon_{sol} \tilde{B}_{sat}. \quad (1)$$

A similar definition allows one to define an efficiency along the divertor leg ε_{leg} and the magnetic field along the leg $\tilde{B}_{leg} = \varepsilon_{leg} \tilde{B}_{sat}$. Part I claimed that this also gives an order of magnitude estimate for the flux surface averaged RMP in the SOL, even though this seems to ignore the spatial variation of the perturbation and the relative weight of the resonant spectral component that is assumed to be necessary for ELM control. This article, Part II, provides the justification for and qualifications of that claim by determining a more accurate expression for the RMP amplitude.

In this article, the spatial structure of the magnetic field perturbation near the X-point is used to develop an approximation for the spectrum that is valid near the separatrix. Pioneering approaches to determination of the resonant spectrum [30–32] have shown that the field must be specified over the entire separatrix. A novel feature of the SOL perturbation is that it is largest near the X-point, and this allows one to obtain an expression that depends weakly on the field far from the X-point. It is shown that the SOL current-generated magnetic perturbation has a relatively large resonant spectral component as long as the SOL current, which propagates along field lines in the scrape-off layer, is well-aligned with the field lines inside the separatrix. The actual RMP amplitude varies radially from a small value in the core to a large value at the edge. Thus, the claim is really that the estimate in Eq. 1 is valid for a certain range of flux surfaces sufficiently close to the separatrix.

The notation, geometry and the structure of the SOL current are described in detail in Part I (Ref. [4]) and briefly reviewed in Sec. II of this article. The central assumption is that the parallel current that is produced will flow along the field lines for a substantial distance from the divertor target plate because dissipative effects are relatively weak [2]. The spatial structure of the resulting vector potential and magnetic field is analytically derived and computed in Sec. III. Outside of the current channel, the field is well described by the effective surface current flowing along the separatrix. The “far-field” result derived in Sec. IIIB is the essential ingredient needed to evaluate the spectrum and limiting forms for the magnetic field are explicitly given in Sec. IIIC. Section IIID shows that the vector potential of a true surface current localized to a thin channel near a single flux surface has a very simple form near the X-point if the target plate is sufficiently far away. Integrating

this result across flux surfaces, as in Sec. III E, also yields the vector potential generated by a current density channel of arbitrary thickness in closed form. Just outside of the current channel, the SOL field has the same amplitude determined by the efficiency ε_{sol} in Part I. The Fourier spectrum of the field is computed in magnetic coordinates in Section IV. The spectrum is calculated asymptotically, both for a poloidally localized perturbation in Sec. IV B and for the SOL current perturbation in Sec. IV C. The quasilinear stochastic transport that would be generated in the absence of shielding effects is estimated in Sec. V. Finally, the results are discussed and summarized in Sec. VI.

II. DIVERTOR LEG & SOL CURRENTS

The conventions for notation and divertor geometry are substantially the same as in Part I. The divertor region of a large aspect ratio tokamak is considered with the coordinate system shown in Fig. 1. The x -axis lies along the outer divertor leg and the y -axis lies along the outer SOL branch of the the separatrix. The toroidal coordinate ζ is directed out of the page for a right-handed coordinate system

Near the X-point, the field line motion is entirely determined by the poloidal flux function $\Psi_p = RB'_p xy$. The two constants of the field line motion can be taken to be a normalized poloidal flux near the X-point and the field line label

$$\psi = xy \qquad \zeta_0 = \zeta - q_* \log \sqrt{|y/x|}. \quad (2)$$

The dimensionless parameter

$$q_* = B_t / RB'_p \quad (3)$$

regulates the ratio of toroidal to poloidal motion near the X-point. The poloidal coordinate that is canonically conjugate to ψ is

$$\theta = \log \sqrt{|y/x|}, \quad (4)$$

in the sense that $(\nabla\psi \times \nabla\theta) \cdot R\nabla\zeta = 1$. This coordinate provides a simple description of the field line motion since $d\zeta/d\theta = q_*$, but $\nabla\theta$ becomes nearly degenerate with $\nabla\psi$ far from the X-point. The variable that is orthogonal to ψ is the conformal conjugate

$$\tau = (y^2 - x^2)/2. \quad (5)$$

The parallel current density is must larger than the other components, so that charge continuity implies $0 = \nabla \cdot \mathbf{J} \simeq \mathbf{B} \cdot \nabla J_{\parallel} / B$. Hence, the parallel current density within a flux tube J_{\parallel} / B must essentially be constant along a magnetic field line. Assuming that the aspect ratio is large, one can approximate $\mathbf{B} \cdot \nabla J_{\parallel} \simeq 0$. Thus, the parallel current density can only depend on the two constants of the field line motion in Eq. 2. Because the current density must be periodic in ζ and therefore ζ_0 , it can be Fourier expanded in toroidal harmonics n . As in Part I, the Fourier harmonics are treated individually, so that one can assume

$$J_{\parallel}(\psi, \zeta_0) = J(\psi) \cos[n\zeta_0 + \chi(\psi)]. \quad (6)$$

In this article, the phase of the current density will be redefined in a manner that allows one to treat the divertor leg and SOL simultaneously. Introduce the parameters k_x, k_y and χ so that the perturbation phase is always written as either

$$\varphi(x) = n\zeta + m_* \log |k_x x| + \chi \quad (7a)$$

as a function of x , or

$$\varphi(y) = n\zeta - m_* \log |k_y y| + \chi \quad (7b)$$

as a function of y . One can choose χ to have the same value in both expressions in Eq. 7 by absorbing any ψ dependence into the parameters k_x, k_y . Then, since $xy = \psi$, the two parameters must be related via $k_x k_y = 1/|\psi|$.

The phase structure of J_{\parallel} in the SOL is sensitive to the phasing of the bias at the target plate. Two limiting cases for orthogonal target plates with radially constant target plate phase profiles were identified in Part I. The conceptual limits of “long” vs. “short” divertor legs naturally arises when considering the divertor leg length ℓ relative to the distance of the current channel δr from the strike point. Part I found that the SOL current drive efficiency is enhanced for short legs, so it can be useful to generate this phasing. However, the terminology only strictly applies for orthogonal target plates, and the two extremes can be continuously connected by varying the angle of the plates with respect to the magnetic field. Although ITER has relatively long legs, the inwardly-inclined non-orthogonal target plates imply that the outer SOL may be closer to the short leg phasing. Either case may also be achievable in a flexible biasing scenario by varying the phasing on the target plate radially as well as toroidally.

The discussion in this article technically focuses on the case of “long” legs (Fig. 4(a) of Ref. [4]). This case provides a natural simplification in that the fields local to the target plate can be neglected. In this case, the target plate runs along y perpendicular to the divertor leg at $x = \ell$. The choice $k_x = 1/\ell$ implies that χ is the phase at the target plate and that $k_y = |\ell/\psi|$. Many of the results in this article can also be used “short” divertor legs (Fig. 4(b) of Ref. [4]). In the limiting case of zero divertor leg length, the target plate runs radially along the half-line $x = y > 0$. In this case, the phase is constant along the line $x = y$ and the choice $k_x = k_y = 1/\sqrt{|\psi|}$ implies that χ is the phase at the target. Our conventions allow this phasing to be described, but additional perturbation fields considered in Appendix C must also be taken into account.

The surface current is defined by integrating the current density over the distance orthogonal to flux surfaces:

$$K_{\parallel}(\tau, \zeta) = \int J_{\parallel}(\psi, \tau, \zeta) d\psi / |\nabla\psi|. \quad (8)$$

Flux expansion causes the surface current to increase near the X-point and decrease further away since $|\nabla\psi| = r$. Assume that distance of the current channel from the X-point at the target is $r_t = \ell$ for long legs or $r_t = \sqrt{2\delta\psi}$ for short legs. The surface current is largest at the distance of closest approach to the X-point $r_X = \sqrt{2\delta\psi} = \sqrt{2\ell\delta r}$ and yields an amplification of $\sqrt{\ell/2\delta r}$ for the long legs. This directly corresponds to the greater width that current can be driven over the target plate for short legs.

Part I assumed that for ITER, where $\ell = 100$ cm, the e -folding length for J_{sat} near the strike point is $\lambda \simeq 2 - 3$ cm. Using this as an estimate of δr yields $r_X = 20 - 25$ cm and yields an X-point enhancement of $6 - 7$. The surface current is weakest at the midplane where $|\nabla\psi| = \kappa a$ where κ is the elongation and a is the minor radius at the outer midplane. For ITER, where $a = 200$ cm and the cross-sectional area is $S = 21.9$ m², we estimate that $\kappa \simeq S/\pi a^2 = 1.74$ which yields a reduction by a factor of $\ell/\kappa a = 1/3.5$. Thus, the characteristic estimate \tilde{B}_{sol} in Eq. 1 provides an estimate of the average between these two extremes.

The current drive efficiency in Eq. 1 is defined by the ratio of amplitude of the net surface current density to the maximum value that can be generated at the target. The definition for the SOL is thus

$$\varepsilon_{sol} = |rK_{\parallel}|/r_t K_{sat}, \quad (9)$$

as $\tau \rightarrow \infty$ and the amplitude is the maximum value of the current over toroidal angle ζ . The same definition is given for the divertor leg efficiency ε_{leg} as $\tau \rightarrow -\infty$.

III. NEAR X-POINT PERTURBATION

A. Green's function approach

The spatial structure of the magnetic perturbation is determined by the static Maxwell's equation $\nabla \times \mathbf{B} = 4\pi\mathbf{J}/c$, which can be solved for the vector potential $\nabla \times \mathbf{A} = \mathbf{B}$. Because the poloidal field vanishes at the X-point, the weak poloidal component of the parallel current can be neglected through first order in r/R . This implies that the “slab” approximation $\nabla_{\perp}^2 A_{\parallel} = -4\pi J_{\parallel}/c$, is also accurate through first order. The solution for the vector potential in slab geometry can formally be written as

$$\tilde{A}_{\parallel}(\mathbf{x}) = - \int d^2x' \log |\mathbf{x} - \mathbf{x}'|^2 J_{\parallel}(\mathbf{x}')/c. \quad (10)$$

For observation points that lie at distances beyond the thickness of the area over which the current density is large, the effect of the detailed radial structure of the current distribution will be smoothed by the Green's function of the Laplace operator. In this case, the approximation that the current lies on a surface of constant $\delta\psi$ will yield sufficient accuracy. For the case of a surface current, the solution becomes

$$\tilde{A}_{\parallel}(\mathbf{x}) = - \int d\ell_p \log |\mathbf{x} - \mathbf{x}'(\ell_p)|^2 K_{\parallel}(\ell_p)/c, \quad (11)$$

where ℓ_p is the poloidal path length along the surface at constant ζ . When parameterized as a function of y along the separatrix or of x along the divertor leg, the integrand takes the form $\int K_{\parallel} d\ell_p = \int K_{\parallel} r dy/y = \int K_{\parallel} r dx/x$.

The conformal invariance of the Laplace operator causes the slab Green's function to simplify in the complex coordinates $z = x + iy$ and $\bar{z} = x - iy$. In this article, z will *not* be used as a third coordinate.

B. Far-field vector potential

The magnetic field generated along the separatrix has a robust form for a wide variety of configurations, as long as the observation point is not close enough to the separatrix to

observe the detailed structure of the current source. In this case, the volume current density can be approximated by a surface current density located at position $\delta\psi$. When $r \gg \sqrt{2\delta\psi}$, even the detailed path of the surface current near the X-point can be neglected because the excursion of the path of the surface current from the x and y axes will be negligible, and the integral in Eq. 11 will break into two integrals over the axes of Fig. 1. Thus, the vector potential can be written as

$$\tilde{A}_{\parallel} = \tilde{A}_{sol} + \tilde{A}_{leg}, \quad (12)$$

where the first term \tilde{A}_{sol} is the contribution from the SOL (upper branch), and the second term \tilde{A}_{leg} is the contribution from the divertor leg (lower branch). If the observation point is still close enough to the current source, then the limits of integration can be sent to infinity. Physically, this neglects the curvature of the flux surfaces, as well as the precise way in which the current is delivered from the external world to the plasma region.

Since the SOL and leg contributions take nearly identical forms, we first treat the SOL term. The required integral (Eq. 11) can be written as

$$\tilde{A}_{sol} = \frac{\tilde{B}_{sol} r_t}{2\pi} \text{Re } e^{i(n\zeta + \chi)} [\mathcal{A}_{m_*}^{sol}(z) + \mathcal{A}_{m_*}^{sol}(\bar{z})] \quad (13a)$$

$$\mathcal{A}_{m_*}^{sol}(z) = - \int_0^{\infty} \frac{dy'}{y'} (k_y y')^{-im_*} \log(y' + iz) \quad (13b)$$

where Re denotes the real part and $\tilde{B}_{sol} = 2\pi\epsilon_{sol}K_{sol}/c$ is the characteristic SOL field strength. Equation 13b can be integrated by parts to find the more tractable form

$$\mathcal{A}_{m_*}^{sol}(z) = - \int_0^{\infty} \frac{dy'}{im_*} (k_y y')^{-im_*} (y' + iz)^{-1}. \quad (13c)$$

However, this is only true if one neglects the total derivative term that should arise to give a contribution at the endpoints at 0 and ∞ (and treated explicitly in Appendix C). For the infinite endpoint, such terms lead to a negligible constant, just as in the case of a uniform density along an infinite line. The more exact treatment of Sec. IIID proves that, for each surface in the current density channel, the term arising near the X-point exactly cancels a corresponding contribution from the divertor leg. Thus, these terms must be actually be neglected here.

The integral in Eq. 13c evaluates to

$$\mathcal{A}_{m_*}^{sol}(z) = \frac{\pi(ik_y z)^{-im_*}}{m_* \sinh m_* \pi}. \quad (14)$$

It is evaluated by contour integration in the complex plane in Appendix A. The vector potential perturbation generated by the SOL current is simply

$$\tilde{A}_{sol} = \frac{\tilde{B}_{sol} r_t}{m_*} \operatorname{Re} \frac{\cos(\varphi_{sol} + im_* \vartheta_{sol})}{\sinh m_* \pi} \quad (15a)$$

$$= \frac{\tilde{B}_{sol} r_t}{m_*} \frac{\cosh m_* \vartheta_{sol}}{\sinh m_* \pi} \cos \varphi_{sol} \quad (15b)$$

and

$$\vartheta_{sol} = \arg(ik_y z) \quad (16a)$$

$$\varphi_{sol} = n\zeta - m_* \log |k_y r| + \chi. \quad (16b)$$

The divertor leg integral can similarly be written as

$$\tilde{A}_{leg} = \frac{\tilde{B}_{leg} r_t}{2\pi} \operatorname{Re} e^{i(n\zeta + \chi)} [\mathcal{A}_{m_*}^{leg}(z) + \mathcal{A}_{m_*}^{leg}(\bar{z})] \quad (17a)$$

$$\mathcal{A}_{m_*}^{leg}(z) = \int_0^\infty \frac{dx'}{x'} (k_x x')^{im_*} \log(x' - z) \quad (17b)$$

$$= - \int_0^\infty \frac{dy'}{im_*} (k_x x')^{im_*} (x' - z)^{-1}. \quad (17c)$$

where $\tilde{B}_{leg} = 2\pi\epsilon_{leg} K_{sat}/c$ is the characteristic divertor field strength. The last line results after again neglecting the total derivative term. These additional terms depend on the way that the current paths are closed near the divertor target and can actually vanish in certain situations. The case of a divertor leg of finite length is treated in Appendix C. The contribution of the additional terms is small near the X-point and their contribution far from the X-point is not highly resonant. Thus, these terms will be neglected here.

The integral Eq. 18 yields

$$\mathcal{A}_{m_*}^{leg}(z) = \frac{\pi(-k_x z)^{im_*}}{m_* \sinh m_* \pi}. \quad (18)$$

Thus, \tilde{A}_{leg} can be written in the same manner as Eq. 15 with the new definitions

$$\vartheta_{leg} = \arg(-k_x z) \quad (19a)$$

$$\varphi_{leg} = n\zeta + m_* \log |k_x r| + \chi. \quad (19b)$$

Color contours of the vector potential are shown in Fig. 2(a) for the balanced case $\tilde{B}_{leg} = \tilde{B}_{sol}$ appropriate for a true surface current along the separatrix. The parameters are $m_* = 4.5$ and $\ell/\delta r = 25$, where here ℓ is only needed to determine the phase to logarithmic accuracy. Large amplitude oscillations along the separatrix are clearly seen. These oscillations are in phase with closed field lines just across the separatrix.

C. Far-field magnetic perturbation

Given the vector potential, the derivation of the magnetic perturbation is a routine calculation. The steps are efficiently performed in complex coordinates in Appendix B. The components of physical interest are the normal and the tangential components, which can be written in the compact form

$$\tilde{B}_{\hat{\psi}} - i\tilde{B}_{\hat{\tau}} = 2i(\bar{z}/r)\partial_z A \quad (20a)$$

$$\tilde{B}_{\hat{\psi}} = \mathbf{B} \cdot \nabla \psi / |\nabla \psi| = \mathbf{B} \cdot \nabla \psi / r \quad (20b)$$

$$\tilde{B}_{\hat{\tau}} = \mathbf{B} \cdot \nabla \tau / |\nabla \tau| = \mathbf{B} \cdot \nabla \tau / r. \quad (20c)$$

Color contours of the tangential and normal components of the corresponding magnetic perturbation are shown in Fig. 2(b) and (c). Far enough away from the X-point, the principal terms come from the SOL contribution to Eq. 12:

$$B_{\hat{\psi}} - iB_{\hat{\tau}} = \frac{\tilde{B}_{sol} r_t}{2ir} \sum_{\nu=\pm n} e^{i\nu(\zeta+i\chi)} \frac{\bar{z}}{z} \frac{(ik_y z)^{-i\nu q_*}}{\sinh \nu q_* \pi} \quad (21a)$$

$$= \frac{\tilde{B}_{sol} r_t}{r} \frac{\sin(\varphi'_{sol} + i\vartheta_{sol})}{\sinh m_* \pi} \quad (21b)$$

$$\varphi'_{sol} = \varphi_{sol} + \arg \bar{z}/z. \quad (21c)$$

The normal and tangential components evaluate to

$$\tilde{B}_{\hat{\psi}} = \frac{\tilde{B}_{sol} r_t}{r} \frac{\cosh m_* \vartheta_{sol}}{\sinh m_* \pi} \sin \varphi'_{sol} \quad (22a)$$

$$\tilde{B}_{\hat{\tau}} = -\frac{\tilde{B}_{sol} r_t}{r} \frac{\sinh m_* \vartheta_{sol}}{\sinh m_* \pi} \cos \varphi'_{sol}. \quad (22b)$$

Along the upper branch of the separatrix that is close to the perturbation current ($x = 0$, $y > 0$), far above the X-point ($x \ll y$), one finds the simple result that $\tilde{B} \sim \tilde{B}_{sol} r_t / r$ due to the radial dependence of the surface current. Using the limit $\vartheta_{sol} \rightarrow \pi x / |x|$ allows one to find that

$$\tilde{B}_{\hat{\psi}} \rightarrow \frac{\tilde{B}_{sol} r_t}{r} \coth m_* \pi \sin \varphi'_{sol} \quad (23a)$$

$$\tilde{B}_{\hat{\tau}} \rightarrow -\frac{x}{|x|} \frac{\tilde{B}_{sol} r_t}{r} \cos \varphi'_{sol}. \quad (23b)$$

The contribution to the other branches of the separatrix are much smaller at large m_* . Along the opposite upper branch of the separatrix that is far from the SOL current ($x < 0$,

$y = 0$), far above the X-point ($-x \gg y$) where $\vartheta_{sol} \rightarrow \pi/2$, the result is

$$\tilde{B}_{\hat{\psi}} \rightarrow \frac{\tilde{B}_{sol} r_t}{r} \frac{\cosh m_* \pi/2}{\sinh m_* \pi} \sin \varphi'_{sol} \quad (24a)$$

$$\tilde{B}_{\hat{\tau}} \rightarrow -\frac{\tilde{B}_{sol} r_t}{r} \frac{\sinh m_* \pi/2}{\sinh m_* \pi} \cos \varphi'_{sol}. \quad (24b)$$

If $m_* \pi/2 > 1$, the perturbation field must increase rapidly from the far side to the near side. The contribution to the lower branch along the divertor leg has the same magnitude with opposite sign since $\vartheta \rightarrow -\pi/2$. The contribution to the diametrically opposed branch ($x = 0, y < 0$) is even smaller and scales like $\sim \exp(-|m_* \pi|)$.

The contribution from the divertor leg can be expanded in a similar fashion. In this case, the results for the outer upper separatrix (the outer SOL $x = 0, y > 0$) are similar in magnitude to Eqs. 24 (a) and (b). For large m_* , this is a factor $\exp(-|m_* \pi/2|)$ smaller than the corresponding contribution from the SOL current. Hence, along the separatrix, the divertor leg field can be neglected at large m_* if the SOL surface current drive is not exponentially small. In fact, if the entire orthogonal target plate is biased at the same phase radially, the SOL current drive is exponentially smaller. Interestingly enough, for long divertor legs the SOL current is smaller by almost the same factor (Part I, Eq. 39) and the SOL field strength only dominates by the factor $\sqrt{|2\pi m_*|}$. For short legs, the efficiency at large m_* is better and the product scales as $\sqrt{|m_* \pi|} \exp(|m_* \pi/4|)$. Thus, even at large m_* the SOL perturbation will dominate the divertor leg perturbation for short legs.

D. Near-field of a narrow current layer

The result can be written in a similar form even when the observation point is close enough to the X-point to resolve the shape of the path of the surface current. In this section, we treat the case of a true surface current along the path $\delta\psi = xy$. In this case, the efficiencies are equal and the normalization field becomes $\tilde{B}_0 \equiv \tilde{B}_{sol} = \tilde{B}_{leg}$. The argument of the logarithm in Eq. 11 can be expanded as

$$(x' - x)^2 + (\delta\psi/x' - y)^2 = (x' - z_+)(x' - z_-)(x' - \bar{z}_+)(x' - \bar{z}_-)/x'^2. \quad (25)$$

where the z_{\pm} are defined as the two solutions for x' of the equation $0 = x'^2 - zx' + i\delta\psi$; i.e.

$$z_{\pm} = z/2 \pm \sqrt{(z/2)^2 - i\delta\psi}. \quad (26)$$

In this case, the total derivative term only contributes a negligible constant and Eq. 11 becomes

$$\tilde{A}_{\parallel} = \frac{\tilde{B}_0 r_t}{2\pi} \text{Re} \sum_{\sigma=\pm} e^{i(n\zeta+\chi)} [\mathcal{A}_{m_*}(z_{\sigma}) + \mathcal{A}_{m_*}(\bar{z}_{\sigma})] \quad (27a)$$

where

$$\mathcal{A}_{m_*}(z) = - \int_0^{\infty} \frac{dx'}{x'} (k_x x')^{im_*} \log(x' - z_{\pm}) \quad (27b)$$

$$= \frac{\pi(-k_x z_{\pm})^{im_*}}{m_* \sinh m_* \pi}. \quad (27c)$$

The definitions

$$r_{\pm} = |z_{\pm}| \quad (28a)$$

$$\vartheta_{\pm} = \arg(-k_x z_{\pm}) \quad (28b)$$

$$\varphi_{\pm} = n\zeta + m_* \log |k_x r_{\pm}| + \chi \quad (28c)$$

allow the result to be written as sum over terms in Eq. 15:

$$\tilde{A}_{\parallel} = \frac{\tilde{B}_0 r_t}{m_*} \sum_{\sigma=\pm} \frac{\cosh m_* \vartheta_{\sigma}}{\sinh m_* \pi} \cos \varphi_{\sigma}. \quad (29)$$

When $\delta\psi < r^2/4$, the roots z_{\pm} take the limits z and $\delta\psi/iz$, and the limiting result is the same as that of Eq. 15. Contours of the vector potential perturbation are plotted in Fig. 3(a). The additional terms are clearly small for distances of order $2\sqrt{\delta\psi}$ away from the location of the surface current as can be seen by comparing Fig. 2 to 3.

The magnetic field can be derived by differentiation, which results in a sum over the roots z_{\pm} of terms in the exact same form as Eqs. 21 and 22. These results are displayed as color contours in Fig. 3(b) and (c).

E. Near-field of a wide current layer

For the case of a step-wise constant current amplitude driven at the target, one can again derive an exact result for the perturbation to the vector potential in closed form. Here we treat the case of long legs, and the results are used to construct the vector potential in Fig. 4 (a).

One simply needs to integrate the previous result in Eq. 27 over the width of the current layer $\psi \in [\psi_a, \psi_b]$. In fact, one can integrate over both roots at the same time. The indefinite integral is

$$\mathcal{A}' = \int d\psi \int_0^\infty \frac{dx'}{x'} (k_x x')^{im_*-1} \log(x'^2 - zx' + i\psi). \quad (30a)$$

Integration over ψ leads to

$$\mathcal{A}' = -i \int_0^\infty \frac{dx'}{x'} (k_x x')^{im_*-1} \times (x'^2 - zx' + i\psi) \log(x'^2 - zx' + i\psi). \quad (30b)$$

In this form, one can factor the argument of the logarithm over the roots z_\pm . For each factor, one can then determine

$$\mathcal{A}'_{m_*}(z_\pm) = -ik_x \int_0^\infty dx' (k_x x')^{im_*-1} \times (x'^2 - zx' + i\psi) \log(x' - z_\pm) \quad (31a)$$

$$= \frac{\pi(-k_x z_\pm)^{im_*}}{\sinh(m_*\pi)} \left(\frac{(-z_\pm)^2}{im_* + 2} - \frac{zz_\pm}{im_* + 1} + \frac{i\psi}{im_*} \right) \quad (31b)$$

$$= -\frac{\pi(-k_x z_\pm)^{im_*}}{(im_* + 1) \sinh(m_*\pi)} \left(\frac{(-z_\pm)^2}{im_* + 2} - \frac{i\psi}{im_*} \right). \quad (31c)$$

Note, however, that due to Eq. 30a the contribution from the complex conjugate root is $\mathcal{B}'_{m_*}(\bar{z}_\pm) \equiv -\mathcal{A}'_{m_*}(\bar{z}_\pm, -\psi)$. The indefinite integral for the vector potential is the sum

$$\tilde{A}(\psi) = \frac{\tilde{B}_{leg} r_t}{2\pi} \text{Re} \sum_{\sigma=\pm} e^{i(n\zeta+\chi)} [\mathcal{A}'_{m_*}(z_\sigma) + \mathcal{B}'_{m_*}(\bar{z}_\sigma)]. \quad (32)$$

Outside of the current layer, the answer is a simple difference between indefinite forms $\tilde{A}_\parallel = \tilde{A}(\psi_b) - \tilde{A}(\psi_a)$. In the far-field, $r^2 > 4\psi$, one finds that $z_\pm \rightarrow z, i\psi/z$, which yields the limits for the leg

$$\mathcal{A}'_{m_*}(z_+)|_{\psi_a}^{\psi_b} \simeq (\psi_b - \psi_a) \left(\frac{\pi(-k_x z)^{im_*}}{m_* \sinh \pi m_*} \right) \quad (33a)$$

and for the SOL

$$\mathcal{A}'_{m_*}(z_-)|_{\psi_a}^{\psi_b} \simeq \frac{\psi}{im_* + 1} \left(\frac{\pi(iz/k_x \psi)^{-im_*}}{m_* \sinh \pi m_*} \right) \Big|_{\psi_a}^{\psi_b}. \quad (33b)$$

For a thin current channel, the magnitude of the separatrix contribution is the same as that of the leg. For wide separations, $\psi_b \gg \psi_a$ and the inner point can be neglected. Hence, the far-field SOL perturbation is smaller by $\sim 1/\sqrt{1+m_*^2}$ for distributions thicker than the coherence width.

Within the current layer, the Green's function has a branch cut when the radial position xy is equal to the value of ψ in the layer. The nonzero jump across the layer produces the particular solution that satisfies $\nabla^2 A \neq 0$. The integral over ψ must actually be defined by the principal part across the branch cut

$$\mathcal{P} \int_{\psi_a}^{\psi_b} = \int_{\psi_+}^{\psi_b} + \int_{\psi_a}^{\psi_-} \quad (34a)$$

where $\psi_{\pm} = \lim_{\epsilon \rightarrow 0+} xy \pm \epsilon$. In the current layer, this yields the result

$$\tilde{A}_{\parallel} = \tilde{A} \Big|_{\psi_a}^{\psi_b} - \tilde{A} \Big|_{\psi_-}^{\psi_+}. \quad (34b)$$

The magnetic field is again found by differentiation. There are now quite a few more terms that must be summed to yield Fig. 4 (b) and (c).

IV. NEAR SEPARATRIX SPECTRUM

A. Definition in canonical coordinates

The Fourier spectrum of the perturbation in canonical coordinates is needed for the determination of the resonant components of the spectrum. The first step is to define a new set of canonical coordinates with a poloidal angle that is normalized to 2π , and this, in turn, requires an estimation of the safety factor for field lines inside of the separatrix. The leading dependence of the safety factor on the radial distance from the separatrix is logarithmic and the leading term only requires the field line motion in X-point region. Assume that the field line begins at the point $y = -x = \sqrt{|\psi|}$. In order to travel half of a poloidal circuit, the field line must travel to a point $y = b$ which we estimate to be on order of the minor radius a . The toroidal angle traversed in this process can be expressed as $\Delta\zeta = q_* \log(b/\sqrt{|\psi|})$. This yields the safety factor of the near-separatrix trajectory

$$q = 2\Delta\zeta/2\pi = (q_*/2\pi) \log(|b^2/\psi|). \quad (35)$$

The next order term is a constant that depends on the contribution of the region far from the X-point. In general, b can be redefined to make this expression accurate to order unity by absorbing this constant. We call this distance “the separatrix scale length.” Even in the case of multiple X-points, this expression for q can be made exact up to order unity by taking the average of the q_* ’s for each X-point and an appropriate choice of b (see Ref. [31]).

Given the safety factor, one can define canonical action-angle coordinates along separatrix via the near X-point forms

$$\Theta = \theta q_*/q = (q_*/q) \log \sqrt{|y/x|} \quad (36a)$$

$$\Psi_t = \int q d\psi/q_* = (\psi/2\pi)(\log |b^2/\psi| + 1) \quad (36b)$$

In these coordinates, the Jacobian satisfies $\mathcal{J} = 1/(\nabla\Psi_t \times \nabla\Theta) \cdot R\nabla\zeta = 1$. Here, Θ is the poloidal angle and Ψ_t is the normalized *toroidal* flux near the X-point since $d\Psi_p/d\Psi_t = d\zeta/d\Theta = q$.

The Fourier harmonics of the normal field perturbation can be defined by the surface integral

$$\tilde{B}_{mn} = \oint e^{i(n\zeta - m\Theta)} \mathbf{B} \cdot d^2\mathbf{a}/S \quad (37)$$

where $S = \oint |d^2\mathbf{a}| \simeq (2\pi)^2 aR$ is the area of the flux surface. Note that exponential Fourier harmonics are a factor of 1/2 smaller than the sin and cosine harmonics used in Refs. [20, 21, 23, 24].

The normal field is simply related to the perturbed poloidal flux via $\mathcal{J}\mathbf{B} \cdot \nabla\Psi = \partial_\Theta A_\zeta$. If we define

$$\tilde{A}_{mn} = \oint e^{i(n\zeta - m\Theta)} \tilde{A}_\parallel d\Theta d\zeta / (2\pi)^2 \quad (38)$$

then

$$\tilde{B}_{mn} = im \frac{(2\pi)^2 R}{S} \tilde{A}_{mn} \simeq \frac{im}{a} \tilde{A}_{mn}. \quad (39)$$

Note that, for a given resonant perturbation in normal field, the perturbed potential $\tilde{A}_{mn} \sim 1/m \sim 1/nq$, and thus must vanish as $q \rightarrow \infty$ as the separatrix is approached.

Which part of the trajectory contributes most to the resonance in the definition of the resonant spectrum in Eqs. 37 and 38? The answer is unique, but can appear to raise a paradox when switching between coordinate systems and definitions. The simple answer is that, near the X-point, the differential area element, $d^2\mathbf{a} = \hat{\mathbf{x}}dydz - \hat{\mathbf{y}}dzdx$, is equally

sensitive to a given normal field as any other part of the flux surface. However, in canonical coordinates, the area element is $d^2\mathbf{a} = \nabla\Psi\mathcal{J}d\Theta d\zeta$, and, because $|\nabla\psi| \sim r$, the area element now appears to be weighted more heavily at positions further from the X-point. By definition, the Jacobian \mathcal{J} is non-singular in canonical coordinates and requires no special treatment near the X-point. Of course, in real space this weighting is canceled by the fact that $d\Theta \propto d\ell_p/B_p \propto d\log|x/y|$. The same considerations hold true for the definition that involves the vector potential. It is clear that $d\Theta$ represents uniform weighting in magnetic coordinates, while, in real space, the X-point appears weighted more heavily. This apparent paradox is resolved by the fact that the vector potential is always one power of r larger than the field. For instance, due to gauge freedom $A_\zeta(\zeta)$ does not generate a magnetic perturbation, and the first contribution comes from terms that scale as r . Thus, the two definitions are equivalent.

For a generic perturbation, given the magnetic field in the neighborhood of a specific point, it is only possible to obtain a rough estimate for the flux surface average. In order to see the effect of a generic perturbation near the X-point, Taylor expand the vector potential in terms of the powers $x^j y^k$ and drop the irrelevant constant gauge term. In the vicinity of the X-point, $xy = \psi$ and $d\Theta = (q_*/q)dy/y$, so that

$$\int x^j y^k e^{-im\Theta} d\Theta = \frac{q_*}{q} \int x^j y^{k-1} |x/y|^{im_*/2} dy \quad (40a)$$

$$= \left(\frac{q_*}{q}\right) \frac{|x/y|^{im_*/2} x^j y^k}{-im_* + (k-j)} \quad (40b)$$

where $m_* = mq_*/q$. The result yields two conclusions. First, because the denominator is complex, it never vanishes unless both $|m_*|$ and $|k-j|$ become small. This implies that the field is broad-band and never achieves a true resonance. Second, the result is clearly largest in magnitude at points far from the X-point, and thus, the result must depend on how the perturbation behaves further away.

A localized current distribution decays far from the source, and allows one to construct an approximation that is valid over the entire trajectory. The spectrum produced by a current source localized near the X-point is determined in the next section. The case of the parallel SOL surface current is similar in that it is largest near the X-point due to the dependence on flux expansion. Section IV C shows that the average is enhanced due to resonance effects and can be determined to within logarithmic accuracy.

B. Spectrum for an X-point localized source

Consider the spectrum of a source that is localized near the X-point. For instance, each lobe of current of the same sign produced by the current drive at the target has total parallel current $I_{lobe} = K_{sat}r_t/m_*$ (Part I, Eq. 26a). Neglecting interference with the other lobes, what is the field produced by such a current source near the X-point? Assume that the observation point is far enough away that the detailed structure of the current can be neglected, but that the current paths close sufficiently far away that the fields decay as $1/r$. Then, the main contribution will be the monopole contribution for the current I_n in the n th Fourier harmonic. If the source is located at position $\{x_j, y_j\}$, the contribution of the harmonic to the perturbed vector potential is

$$\tilde{A}_n = -(I_n/c)e^{-i(n\zeta+\chi_j)} \log[(x-x_j)^2 - (y-y_j)^2]. \quad (41)$$

Since the field far from the X-point is weak, the near X-point behavior will determine the perturbation spectrum. Under these assumptions, the characteristic field at distance a is

$$\tilde{B}_n = 2I_n/ca. \quad (42)$$

The closed field lines are in the region $x < 0, y > 0$. However, one can define the integral in any quadrant by keeping track of the quadrant that the test field line is in. Hence, we introduce the sign of the field line quadrant $\sigma_x = \pm 1, \sigma_y = \pm 1$, so that the path of integration takes place along $z = \rho(\sigma_x/t + i\sigma_y t)$, where $\rho = \sqrt{|\psi|}$ and t parameterizes the path. For closed field lines $\sigma_y = -\sigma_x = 1$. The spectral decomposition in straight field line coordinates is

$$\tilde{A}_{mn} = -\frac{I_n e^{-i\chi_j}}{2\pi c} \frac{q_*}{q} \int_0^\infty dt t^{-im_*-1} \times \log [(\rho t - \sigma_y y_j)^2 + (\rho^2/t - \sigma_x x_j)^2]. \quad (43)$$

This integral is in the same form as Eq. 27. Here we define the two solutions for y of $y^2 - w_j y - i\rho^2$ to be

$$w_{j\pm} = r_{j\pm} e^{i\vartheta_{j\pm}} = w_j/2 \pm \sqrt{(w_j/2)^2 + i\rho^2}. \quad (44)$$

where $w_j = \sigma_y y_j - i\sigma_x x_j$ represents the source position modified by the signs of the flux

surface quadrant. The result is

$$\tilde{A}_{mn} = -\frac{I_n e^{-i\chi_j}}{2cm} \sum_{\sigma=\pm} \frac{(-w_{j\sigma}/\rho)^{-im_*} + (-\bar{w}_{j\sigma}/\rho)^{-im_*}}{\sinh m_* \pi} \quad (45a)$$

$$= -\frac{I_n e^{-i\chi_j}}{cm} \sum_{\sigma=\pm} \frac{\cosh m_* \vartheta_{j\sigma}}{\sinh m_* \pi} \left(\frac{r_{j\sigma}}{\rho} \right)^{-im_*} \quad (45b)$$

with the definition $m = m_* q/q_*$. The flux surface averaged normal magnetic field amplitude is

$$\tilde{B}_{mn} = -i \frac{I_n e^{-i\chi_j}}{ca} \sum_{\sigma=\pm} \frac{\cosh m_* \vartheta_{j\sigma}}{\sinh m_* \pi} \left(\frac{r_{j\sigma}}{\rho} \right)^{-im_*}. \quad (46)$$

The RMP amplitude is given by the value at $m_* = q_* n$ which is equivalent to $m = qn$. Near the separatrix, as $\rho \rightarrow 0$, the $\sigma = +$ contribution is from the outer SOL and $r_{j+}/\rho \rightarrow r_j/\rho$, while the $\sigma = -$ contribution is from the inner SOL and $r_{j-}/\rho \rightarrow \rho/r_j$.

The spectrum is broadband due to the spatial localization of the source. The spectrum decays quickly at large m_* unless the source is close to one of the separatrix branches. Given a source at $r_j = 1$ and a field line at $\psi = 10^{-2}$, Fig. 5(a) plots the amplitude of $|\tilde{B}_{mn}/\tilde{B}_n|$ versus m_* for unit current, and a variety of source locations: $x = 1, y = 0$ (dotted red); $x = 0, y = 0$ (dashed blue); and $x = 0, y = 1$ (solid black). One can clearly see that a more sizable effect is obtained as y_j is raised from far below the X-point where $\vartheta_{j+} \sim 0$ to far above the X-point where $\vartheta_{j+} \sim \pm\pi$. Even when $\vartheta_{j+} = \pm\pi$, $\vartheta_{j-} = \pm\pi/2$ resulting in a negligible contribution from the other side of the trajectory.

The preceding formula in Eq. 46 implies that at large m_* , the perturbation field only efficiently resonates with one of the sides of the separatrix. This yields half the characteristic field B_n as $m \rightarrow \infty$, as confirmed by the asymptote 1/2 for the solid (black) curve in Fig. 5(a). Given the lobe current expression, this leads to the upper limit for the RMP due to the lobe current $\tilde{B}_{nm,lobe} < B_{sat} r_t / m_* a$, which is only fraction of the original maximum. Of course, the actual value is even further reduced, because the upper limit does not account for phase interference from the other lobes.

C. Spectrum for the SOL current source

The field produced by the SOL current density is largest near the X-point and localized in Fourier space. This leads to a logarithmic enhancement of the resonant field over the previous result that can become large near the separatrix. Just as in the determination of

the q profile, the leading dependence of the RMP amplitude is determined by the near X-point field. Although the answer does depend on the properties of the separatrix at further distances where the field is weaker, the effect is to set the next order term, and redefine the scale of the argument of the logarithm. Here, we estimate that this scale is set by the separatrix scale length b , just as it was for the q profile.

The spectrum for an arbitrary current distribution is determined by a sum over thin current channels. Again, we introduce the signs $\sigma_x = \pm 1$, $\sigma_y = \pm 1$, so that the path of integration takes place along the path $z = \sigma_x \rho / t + i \sigma_y \rho t$, where $\rho = \sqrt{|\psi|}$ and t parameterizes the path. The spectrum should be integrated up to a distance on the order of the separatrix scale length b in either direction. In the case of a thin current channel, the vector potential was written as a sum over the roots z_{\pm} . Similarly, the spectrum can be written as a sum

$$\tilde{A}_{mn} = \frac{\tilde{B}_0 r_t}{2m} e^{-i\chi} \sum_{\sigma=\pm} \mathcal{R}_{m_*}^{-m'_*}(k_x z_{\sigma}) + \mathcal{R}_{m_*}^{-m'_*}(k_x \bar{z}_{\sigma}) \quad (47a)$$

$$\tilde{B}_{mn} = \frac{\tilde{B}_0 r_t}{2a} i e^{-i\chi} \sum_{\sigma=\pm} \mathcal{R}_{m_*}^{-m'_*}(k_x z_{\sigma}) + \mathcal{R}_{m_*}^{-m'_*}(k_x \bar{z}_{\sigma}) \quad (47b)$$

over the spectral response functions

$$\mathcal{R}_{m_*}^{m'_*}(z_{\pm}) = \int_{t_0^{-1}}^{t_0} \frac{(-z_{\pm})^{im'_*}}{\sinh m'_* \pi} t^{-im_*} dt. \quad (47c)$$

Here, $t_0 = b/\rho$, $m'_* = nq_*$ and $m_* = mq_*/q$; for an exact relation, one must use $a \equiv S/(2\pi)^2 R$. These expressions are numerically integrated below in order to find the dependance of the spectrum on the position of the current source $\delta\psi$.

To gain analytic insight, consider field lines located at distances greater than $r_X = \sqrt{2\delta\psi}$ from the X-point. At this distance, Eq. 12 is a good approximation for the vector potential and using the efficiency naturally allows one to treat the SOL and divertor leg contributions separately. The largest contribution arises from the SOL contribution to the perturbation and can be expressed as

$$\tilde{B}_{mn}^{sol} = \frac{\tilde{B}_{sol} r_t}{2a} i e^{-i\chi} \left(\mathcal{R}_{m_*}^{m'_*}(ik_y z) + \mathcal{R}_{m_*}^{m'_*}(-ik_y \bar{z}) \right). \quad (48)$$

The SOL spectral response function is

$$\mathcal{R}_{m_*}^{m'_*}(-ik_y z) = (k_y \rho)^{im'_*} \int_{t_0^{-1}}^{t_0} \frac{(i\sigma_x - \sigma_y t^2)^{im'_*}}{\sinh m'_* \pi} t^{-i\mu_* - 1} dt \quad (49)$$

where $\mu_* = m_* + m'_*$. The integral in Eq. 49 evaluates to

$$\mathcal{R}_{m_*}^{m'_*}(-ik_y z) = \frac{(k_y \rho)^{im'_*}}{\sinh m'_* \pi} \left(\frac{\sigma_y}{i\sigma_x} \right)^{i\mu_*/2} f_{m'_*}(iz) B\left(\frac{\sigma_y}{i\sigma_x} t^2; -\frac{i\mu_*}{2}, 1 + im'_*\right) \Big|_{t_0^{-1}}^{t_0} \quad (50a)$$

where $B(z; a, b)$ is the incomplete beta function. Due to the imaginary exponents, proper handling of the complex phases requires the factor

$$f_{m'_*}(iz) = (i\sigma_x - \sigma_y t_0^2)^{im'_*} (1 - \sigma_y t_0^2 / i\sigma_x)^{-im'_*}. \quad (50b)$$

Using the limiting forms of the incomplete beta function for large and small z , the result can be approximated as

$$\mathcal{R}_{m_*}^{m'_*}(-ik_y z) \simeq \frac{(k_y \rho)^{im'_*}}{\sinh m_* \pi} \left(\frac{i\sigma_y}{\sigma_x} \right)^{i\mu_*/2} f_{m'_*}(iz) \left\{ \frac{\Gamma(-i\nu_*/2) \Gamma(-i\mu_*/2)}{2\Gamma(-im'_*)} + \frac{1}{i\nu_*} \left(\frac{i\sigma_y t_0^2}{\sigma_x} \right)^{i\nu_*/2} + \frac{1}{i\mu_*} \left(\frac{i\sigma_y t_0^2}{\sigma_x} \right)^{-i\mu_*/2} \right\} \quad (51)$$

where $\nu_* = m_* - m'_*$. The first two terms in braces in Eq. 51 are due to the effect of the perturbation on the separatrix close to the SOL current, over the range $|y/x| > 1$. The last term is due to the perturbation on the opposite side of the separatrix, far from the SOL current, over the range $|x/y| < 1$.

The oscillation of the current pattern can now resonate with the field line motion on the outer SOL side of the separatrix to create a large amplitude effect. If $m_* \rightarrow m'_* = nq_*$ then the limits $\Gamma[x] \rightarrow 1/x$ and $(z^x - 1)/x \rightarrow \log z$ as $x \rightarrow 0$, yield

$$\mathcal{R}_{m_*}^{m_*}(ik_y z) \simeq \frac{1}{2} \left(\frac{i\sigma_y}{\sigma_x} \right)^{im_*} (i\sigma_x k_y \rho)^{im_*} \log \left(\frac{i\sigma_y t_0^2}{\sigma_x} \right). \quad (52)$$

Substituting this approximation into the expression for the resonant component yields the RMP estimate due to the SOL current

$$\tilde{B}_{m=qn}^{sol} \simeq \frac{\tilde{B}_{sol} r_t}{a} i e^{-i\chi} (k_y \rho)^{im_*} \frac{\cosh m_* \pi}{\sinh m_* \pi} \log(b/\rho). \quad (53)$$

The divertor leg contribution can be expressed as

$$\tilde{B}_{mn}^{leg} = \frac{\tilde{B}_{leg} r_t}{2a} i e^{-i\chi} \left(\mathcal{R}_{m_*}^{-m'_*}(k_x z) + \mathcal{R}_{m_*}^{-m'_*}(k_x \bar{z}) \right). \quad (54)$$

The spectral response function can be obtained from Eqs. 49 and 50 with the replacements $\sigma_x \rightarrow -i\sigma_x$, $\sigma_y \rightarrow -i\sigma_y$, $k_y \rightarrow k_x$, and $m'_* \rightarrow -m'_*$. The resonance with the field line motion

on the outer SOL side of the separatrix is weak $\sim 1/\sin \pi m_*$ at large m_* . In fact, the integral over the inner separatrix now yields a peak on the nonresonant side of the spectrum for $m_* \rightarrow -m'_* = -nq_*$ where

$$\mathcal{R}_{m_*}^{m_*}(k_x z) \simeq -\frac{1}{2} (-i\sigma_y k_x \rho)^{im_*} \log \left(\frac{i\sigma_y}{\sigma_x t_0^2} \right). \quad (55)$$

This leads to a non-resonant peak due to the divertor leg current

$$\tilde{B}_{m=-qn}^{leg} \simeq \frac{\tilde{B}_{leg} r_t}{a} i e^{-i\chi} (k_x \rho)^{-im_*} \frac{\cosh m_* \pi / 2}{\sinh m_* \pi} \log(b/\rho). \quad (56)$$

This contribution is smaller than the SOL term at large m_* by the factor $\exp(-|\pi m_*/2|)$ and has the same reduction found in Sec. IV B for a source that is poloidally localized on the x -axis. Thus, at large m_* , the divertor leg contribution for long divertor legs is negligible compared to the SOL contribution.

The estimate for the amplitude of the resonant spectrum can now be improved over the rough estimate $\tilde{B}_{nm} = \varepsilon \tilde{B}_{sat}$, where ε is the appropriate current drive efficiency. Near the separatrix, the surface averaged RMP has the characteristic behavior

$$\tilde{B}_{res} = \varepsilon \tilde{B}_{sat} (r_t/a) \log(b/\rho) \quad (57)$$

as $\rho/b \rightarrow 0$. The magnitude is smaller by the factor r_t/a , just as in the case of the poloidally localized perturbation. However, in the case of the SOL current, the result is enhanced by the logarithmic factor $\log(b/\rho)$. For field lines near the separatrix, the enhancement will cancel the reduction and the two factors will determine a correction of order unity.

The full expression for the RMP amplitudes depend on the flux surface position ρ/b and the current source position $\delta\psi/\psi$. This dependence typically leads to decreased amplitude at large m_* , but the corrections are weak for parameters of interest. To illustrate the detailed behavior of the results, Fig. 5(a) plots the normalized SOL current generated RMP amplitude $\tilde{B}_{nm}^{sol}/\tilde{B}_{res}$ versus the poloidal test harmonic m_* . In this figure, the poloidal dependence of the current source has been set to $m'_* = nq_* = 3$, $k_x = \ell$ and $k_y = \ell/\psi$. The flux surface positions are $\rho/b = 10^{-1}, 10^{-2}, 10^{-3}$ which yield the enhancement factors 2.3, 4.6, 6.9. Fig. 5(b) plots the normalized divertor leg current generated RMP amplitude $\tilde{B}_{nm}^{div}/\tilde{B}_{res}$ versus the poloidal test harmonic m_* for the same parameters. The result is now peaked on the nonresonant side near $m_* = -3$, but the scale is now on the order of $\cosh(1.5\pi)/\sinh(3\pi) = 8.98 \times 10^{-2}$.

The flux surface averaged resonant spectrum is shown for all $m_* = m'_* = nq_*$ in Fig. 6(a) for the analytic SOL expression (thick lines, Eq. 48) and the divertor leg contribution (thin lines, Eq. 54). This corresponds to current right on the separatrix $\delta\psi = 0$, and the flux surfaces $\rho/b = 10^{-1}, 10^{-2}, 10^{-3}$. The contribution from the SOL clearly dominates at large m_* , while the contribution from the divertor leg is equivalent in magnitude at low m_* . Finally, to explore the dependence on the current position $\delta\psi$, Fig. 6(b) plots a numerical integration of the full expression in Eq. 47b for $\rho/b = 10^{-2}$ and $-\delta\psi/\psi = 0.1, 1, 10$. The results are reduced at large m_* by a factor close to unity.

V. STOCHASTIC TRANSPORT

It is important to understand the consequences of a possible region of stochastic magnetic field at the edge of the plasma. However, the method in which the RMP-ELM controlled plasmas respond to the applied resonant field to produce the observed enhancement of particle transport still requires explanation [23, 24]. For tearing activity that might occur during the non-ideal stages of an internally generated instability, the results in this section can be a good order of magnitude estimate of the stochastic layer that forms. In a rotating plasma, externally applied fields cannot easily excite stable tearing modes and reconnection cannot occur for small amplitude fields [25, 26]. Instead, the applied fields excite ideal internal kink modes and this changes the effective resonant spectrum in a manner that depends on ideal MHD stability [27, 28].

The Fourier harmonics of the vector potential that resonate with the field line motion determine the size of the islands that form, and, when the islands overlap, the size of the chaotic region. For any radial coordinate s , the initial poloidal flux must be of the form $\Psi_p(s)$ and the safety factor must be of the form $q(s)$. If a perturbation to the poloidal flux $\delta\Psi_p = -R\tilde{\mathbf{A}} \cdot d\mathbf{x}/d\zeta \simeq -\tilde{A}_{||}R$ acts to create an island, one can find a new constant of the motion by passing to the helical reference frame of the island where $m = qn$. For a thin island, the new constant is approximately

$$-\bar{\Psi}_p = \frac{\Psi'_p q'}{2q} s^2 + 2|\tilde{A}_{mn}|R \cos(m\Theta - n\zeta + \chi_{mn}) \quad (58)$$

where $q' = dq/ds$, $\Psi'_p = d\Psi_p/ds$. Here, \tilde{A}_{mn} is the amplitude of the (exponential) Fourier

series for the perturbation and χ_{mn} is the phase. The full island width can be computed via

$$\delta s = 4 \sqrt{\left| \frac{2qR\tilde{A}_{mn}}{q'\Psi'_p} \right|} = 4 \sqrt{\left| \frac{2a\tilde{B}_{mn}}{nq'\Psi'_p} \right|}. \quad (59)$$

For this last expression, the appropriate minor radius is $a = S/(2\pi)^2 R$.

The island sizes take a finite limit $\delta r_X = \delta\psi/r_X$ when expressed in terms of distance from the X-point $r_X = \sqrt{2\psi}$. Near the separatrix $dq/d\psi = -q_*/2\pi\psi$, $d\Psi_p/d\psi = B'_p R = B_t/q_*$, and the product $q'\Psi'_p = B_t/2\pi\psi$. This yields the island size in flux space

$$\delta\psi = 8 \sqrt{\left| \pi\psi \frac{qR\tilde{A}_{mn}}{B_t} \right|} = 8 \sqrt{\left| \frac{\pi\psi a R \tilde{B}_{mn}}{n B_t} \right|}. \quad (60)$$

Stochasticity occurs close to the point when islands overlap, so that $|nq'\delta\psi_{st}| = 1$ or $\delta\psi_{st} = |2\pi\psi/m_*|$. This yields the estimate for the size of the stochastic overlap region

$$\delta\psi_{st} = 4 \sqrt{\left| \frac{m_*^2 q R \tilde{A}_{mn}}{\pi B_t} \right|} = 4 \sqrt{\left| \frac{m_* a q_* R \tilde{B}_{mn}}{\pi B_t} \right|}. \quad (61)$$

In order to determine the relative size of the stochastic region, the results must be normalized to the total poloidal flux contained within the separatrix $\Psi_{sep} = aRB_p/2$. The normalized poloidal flux near the separatrix is $\Psi_p/\Psi_{sep} \simeq 2B'_p\psi/B_p a = 2\psi/r_p a$, where, here, the poloidal field scale length is defined by the relation $r_p = B_p/B'_p$. For $\tilde{B}_{mn}/B_t = 10^{-4}$, one obtains a stochastic region on the order of a few percent normalized flux.

In order to estimate the amount of transport produced by the perturbation, one can use the quasilinear approximation for field line diffusion [33]. The quasilinear diffusion coefficient $d_{fl} = \langle \Delta r^2 / \Delta \ell \rangle / 2$ caused by a large number of poloidal harmonics at each toroidal harmonic n is

$$d_{fl} = 2\pi q R \sum_{n=0}^{\infty} \left| \tilde{B}_{mn} / B_t \right|^2 \delta_{m=qn}. \quad (62a)$$

For ITER-like parameters $q_a = 3$, $R = 620$ cm and $\tilde{B}_{mn}/B_t = 10^{-4}$, we find that $d_{fl} = 1.2$ mm²/m. In the pedestal, where $T_{ped} \sim 5$ keV, the transport will be collisionless. In fact, transport in the SOL where the density is reduced to $n_e \sim 10^{13}$ cm⁻³ will be still be approximately collisionless for electrons at $T_{sol} \sim 100$ eV (see estimates in Ref. [23]). Thus, to find an order of magnitude estimate of the particle diffusion caused by the stochastic

field, one can use the simple collisionless result [34] $D = d_{fi}v_t$. For ions with $v_{ti} \sim \sqrt{2T/m_i}$, this estimate yields $D_{ped} \sim 8 \times 10^3 \text{ cm}^2/\text{s}$ and $D_{sol} \sim 1 \times 10^3 \text{ cm}^2/\text{s}$. These levels are of the correct order of magnitude to compete with neoclassical and turbulent particle transport at the edge of an H-mode plasma. On the other hand, collisionless electron diffusion yields an estimate of enhanced thermal conduction $\chi \sim d_{fe}\sqrt{2T/m_e}$ so that $\chi_{ped} \sim 5 \times 10^5 \text{ cm}^2/\text{s}$ and $\chi_{sol} \sim 7 \times 10^4 \text{ cm}^2/\text{s}$. Such an enhancement of electron thermal conduction is apparently unobserved in experiments at DIII-D [18, 23] and JET [19]. This is quite an important result, because the resonant perturbation technique would otherwise produce far too much heat transport.

VI. DISCUSSION & SUMMARY

In Part I (Ref. [4]), the SOL of a high-power tokamak was shown to support an appreciable coherent current both along the divertor leg and in the SOL. Even after quantitatively accounting for destructive phase interference, this current is large enough to drive a significant magnetic perturbation along the separatrix. It was proposed that, after optimizing the biasing geometry to enhance the SOL current, this field could be used to control the edge pressure gradient and achieve the goal of stabilizing ELMs in a high-performance tokamak plasma. The key to this conclusion requires the field to have a large enough flux surface averaged resonant spectral component to achieve the experimentally measured threshold.

In this article, the perturbed vector potential near the X-point was derived in closed form for a divertor with long divertor legs using the slab approximation for the Green's function of the Laplace operator. The perturbed magnetic fields were then calculated from these expressions. The effect of phase mixing for the wide current channels with a step-wise constant amplitude was shown to be well-approximated by the far-field of a thin current channel with different surface current densities along the leg and in the SOL. In agreement with the asymptotic form of the coherent SOL current calculated in Part I, phase interference reduces the perturbation by the factor $1/\sqrt{1+m_*^2}$ for current channels as wide as the coherence width.

The dependence of the resonant spectrum on the flux surface and current source positions was calculated asymptotically close to the separatrix. Only the near X-point behavior was needed because the perturbation fields that were considered decreased further away. For a

source that is localized near the X-point, raising the source from below the X-point near the divertor legs to above the X-point near the SOL produces a much larger effect at large m_* . The SOL current was found to generate a relatively large resonant component over a region near the plasma edge. For the SOL current, the perturbation spectrum is peaked for modes that resonate with the pitch of the current source. Thus, as long as the SOL current is well-aligned with field lines inside the separatrix, this resonant enhancement amplifies the result by a logarithmic factor that can become large near the separatrix. A more accurate estimate for the SOL perturbation is $\tilde{B}_{mn}^{sol} = \tilde{B}_{sol}(r_t/a) \coth m_* \pi \log(b/\rho)$. More detailed results are given in Sec. III.

The RMP is large enough to potentially generate a sizable stochastic edge layer (without consideration of plasma shielding or amplification). If a stochastic layer is driven one should ask whether the parallel current would still generate a coherent perturbation as it travels along the chaotic field lines. For short line lengths, less than a single poloidal turn around the plasma, the field lines follow well-behaved invariant manifolds [23] that do not experience chaotic motion. Here, it was found that the region near the X-point can be sufficient to generate a sizable perturbation. Thus, even if the fields become stochastic, the effect will persist as long as the region near the original X-point retains enough plasma to carry the parallel current.

In conclusion, significant magnetic perturbation effects should be observable if the divertor target plates of a high-power tokamak are biased in a toroidally asymmetric fashion. This analysis has shown that one can generate a large magnetic perturbation field near the X-point, and, with optimization of the biasing geometry, a sizeable SOL current and flux surface averaged RMP. In the future, it would clearly be of interest to simulate the SOL current generation of the RMP field for the finite aspect ratio geometry of a fully shaped toroidal plasma using realistic parallel current distributions. It may be possible for the internal SOL current technique to generate enough RMP amplitude to reduce the edge pressure gradient to the point of ELM stabilization.

Acknowledgments

The authors would like to thank D. D. Ryutov, R. H. Cohen and T. D. Rognlien for extensive discussion. This work was performed under the auspices of the U.S. Department of

Appendix A: Contour integral

The expression for the vector potential in Eq. 13c can be evaluated using contour integration in the complex plane. The required integral is

$$\mathcal{I} = \int_0^\infty dz z^a (z - w)^{-1}. \quad (\text{A1})$$

This integral is also the subject of Appendix C for nontrivial limits of integration. We assume that $\text{Im}(w) \neq 0$ and $\text{Re}(a) < 0$, and take the limit that $\text{Re}(a) \rightarrow -0$. Here, the branch cuts for z and w are assumed to lie along the negative real axis, as usual. Multiplying by $(-1)^a(-1)^{-a}$ then allows us to rotate the branch cut of the integrand to the positive real axis. Now, to evaluate the integral, utilize the so-called “keyhole” contour shown in Fig. 7. Integrate from 0 to ∞ along the real axis, circle the contour once around the Riemann sheet at infinite radius, and then close the contour by integrating back along the real axis from ∞ to 0, and circling the origin. This contour only encloses the pole at $z = w$; hence, the residue theorem yields

$$2\pi i(-w)^a = (e^{-i\pi a} - e^{\pi i a}) \mathcal{I} \quad (\text{A2a})$$

$$\mathcal{I} = -\pi(-w)^a / \sin \pi a. \quad (\text{A2b})$$

Appendix B: Magnetic field in complex coordinates

In this section, the result in Eq. 20a is derived in complex coordinates: $z = x + iy$ and $\bar{z} = x - iy$. For any function $\nabla A = \partial_z A \nabla z + \partial_{\bar{z}} A \nabla \bar{z}$. However, in complex coordinates the metric is completely off diagonal: $(\nabla z)^2 = 0$ and $|\nabla z|^2 = 2$. The cross-product obeys the relation $\nabla z \times \hat{\zeta} = i \nabla \bar{z}$.

Given these simple complex definitions, the magnetic field $\mathbf{B} = \nabla \times \mathbf{A} = \nabla \times A \hat{\zeta}$ is

$$\mathbf{B} = i \partial_z A \nabla z - i \partial_{\bar{z}} A \nabla \bar{z}. \quad (\text{B1})$$

The Cartesian components are

$$B^x - i B^y = \mathbf{B} \cdot \nabla \bar{z} = 2i \partial_z A. \quad (\text{B2})$$

The magnetic field can be computed in the coordinates $\psi + i\tau = -iz^2/2$ by taking the contravariant component

$$B^\psi - iB^\tau = \mathbf{B} \cdot \nabla(i\bar{z}^2/2) = -2\bar{z}\partial_z A. \quad (\text{B3})$$

This leads directly to the normalized result in Eq. 20a.

Appendix C: Fields for finite divertor leg length

If the divertor target is close enough to the plasma, there are additional perturbations to the magnetic field due to the flow of current near the target. In this section, these additional terms will be treated by deriving a more exact expression for the vector potential. Local fields are modified and could potentially increase the perturbation strength for short divertor legs. If the current paths close near the divertor target, the magnetic field will decay more quickly than $1/r$ at large distances. Note that at distances from the source that are further than a toroidal wavelength $2\pi R/n$, the slab approximation will be violated, and the fields will decay as higher multipoles at even faster rates.

Possible long-range terms formally arise from the “endpoints” of the current distribution in the expressions for the vector potential. For instance, in passing from Eq. 17b to Eq. 18, a total derivative term is required to complete the integration by parts, and this term is to be evaluated on the target and near the separatrix. The term that contributes to Eq. 17b or, more generally, to Eq. 27b is

$$\mathcal{A}_{m_*}(z) = - \int_0^{x_t} \frac{dx'}{x'} (x/x_t)^{im_*} \log(x' - z). \quad (\text{C1})$$

where $x_t = \ell$ for long legs and $x_t = \sqrt{\delta\psi}$ for short legs. Integration by parts allows one to express the result as the sum $\mathcal{A}_{m_*}(z) = \mathcal{A}_t(z) + \mathcal{A}'_{m_*}(z)$ where $\mathcal{A}_t(z)$ is the contribution from the total derivative and $\mathcal{A}'_{m_*}(z)$ is the remaining integral.

The integral can be evaluated in closed form in terms of the hypergeometric function $F(a, b; c; z)$. The result is

$$\mathcal{A}'_{m_*}(z) = -\frac{1}{im_*} \int_0^{x_t} dx' (x/x_t)^{im_*} (x' - z)^{-1} \quad (\text{C2a})$$

$$= -\frac{x_t/z}{im_*(1 + im_*)} F(1, 1 + im_*; 2 + im_*; x_t/z) \quad (\text{C2b})$$

$$= \frac{\pi(-z/x_t)^{im_*}}{m_* \sinh \pi m_*} + \frac{1}{m_*^2} F(1, -im_*; 1 - im_*; z/x_t) \quad (\text{C2c})$$

and gives a correction to the perturbation near the target plate due to the fact that the current path changes there. The second line shows that all terms decay quickly at large x_t/z . The first contribution is actually the dipole $\tilde{B} \sim 1/r^2$ term. The last line rewrites the integral as $\int_0^{x_t} = \int_0^\infty - \int_{x_t}^\infty$ to exhibit the answer as a sum of the principal term that was retained $(z/x_t)^{im}$ in Secs. III and IV and a power series in distance from X-point z/x_t that becomes small as $x_t \gg r$.

The total derivative leads to a possible $1/r$ term at the endpoints. The contribution from 0 arises when the current formally flows to $y \rightarrow \infty$, producing negligible field. Thus, one only needs to consider the term at $x = x_t$:

$$\mathcal{A}_t(z) = \frac{1}{im_*} (k_x x_t)^{im_*} \log(x_t - z). \quad (\text{C3})$$

Notice that these term are actually out of phase with the parallel current by $\pi/2$ unlike the contribution from \mathcal{A}' above.

However, there can be a near cancellation at the divertor target plate. At the target, the actual distribution of toroidal current does not simply vanish, but the current paths must close. If direct electrostatic biasing is considered then one must include the physical path in which the actual engineering design feeds and busses supply current to the target region. The simplest such arrangement requires a surface current to flow toroidally along the divertor target itself in order to close the poloidal component of the parallel current density. This is also the natural flow pattern for a thin current channel when generated by internal asymmetries in geometry and thermoelectric potential. Consider a thin surface current density of magnitude K_\parallel flowing above the target at location x_t and y_t , so that in the plasma $\mathbf{J}_{plasma} = K_\parallel \mathbf{b}$. In order for a toroidal current flowing along the target $\mathbf{J}_{target} = J_t \delta(x - x_t) \delta(y - y_t) \hat{\zeta}$ to close the current path via $\nabla \cdot (\mathbf{J}_{target} + \mathbf{J}_{plasma}) = 0$, the target current density must take the form $J_t = -K_\parallel x_t / im_*$. This current is $\pi/2$ out of phase with the plasma current and produces a perturbation that exactly cancels the endpoint contribution arising from Eq. C3.

[1] R. H. Cohen and D. D. Ryutov, Nucl. Fusion **37**, 621 (1993).

[2] D. D. Ryutov, P. Helander and R. H. Cohen, Plasma Phys. Control. Fusion **43**, 1399 (2001).

- [3] G. F. Counsell, R. H. Cohen, P. Helander, D. D. Ryutov and the MAST Team, 30th EPS Conference on Contr. Fusion and Plasma Phys., St. Petersburg, 2003, edited by R. Koch and S. Lebedev (European Physical Society, 2003), Europhysics Conference Abstracts **27A** P-3.202, http://epsppd.epfl.ch/StPetersburg/PDF/P3_202.PDF
- [4] I. Joseph, R. H. Cohen and D. D. Ryutov, "Driving toroidally asymmetric current through the tokamak scrape-off layer, Part I: Potential for ELM suppression," submitted to Phys. Plasmas (2008).
- [5] F. Najmabadi and the ARIES Team, Fusion Eng. Des. **38**, 3 (1997).
- [6] A. S. Kukushkin, H. D. Pacher, G. Federici, G. Janeschitz, A. Loarte, G. W. Pacher, Fusion Eng. Des. **65**, 355 (2003).
- [7] M. Kotschenreuther, P. M. Valanju, S. M. Mahajan and J. C. Wiley, Phys. Plasmas **14**, 072502 (2007).
- [8] G. Federici, A. Loarte and G. Strohmeyer, Plasma Phys. Control. Fusion **45**, 1523 (2003).
- [9] T. E. Evans, C. J. Lasnier, D. N. Hill, A. W. Leonard, M. E. Fenstermacher, T. W. Petrie, M. J. Schaffer Journal of Nuclear Materials **220-222**, 235 (1995).
- [10] M. E. Fenstermacher, A. W. Leonard, P. B. Snyder, J. A. Boedo, N. H. Brooks, R. J. Colchin, D. S. Gray, R. J. Groebner, M. Groth, E.M. Hollmann, C. J. Lasnier, T. H. Osborne, T. W. Petrie, D. L. Rudakov, H. Takahashi, J. G. Watkins, L. Zeng and the DIII-DTeam, Plasma Phys. Control. Fusion **45**, 1597 (2003).
- [11] H. Takahashi, E. D. Fredrickson¹, M. J. Schaffer, M. E. Austin, T. E. Evans, L. L. Lao and J. G. Watkins, Nucl. Fusion **44**, 1075 (2004).
- [12] H. Takahashi, E. D. Fredrickson and M. J. Schaffer, Phys. Rev. Lett. **100**, 205001 (2008).
- [13] H. R. Wilson and R. L. Miller, Phys. Plasmas **6**, 873 (1999).
- [14] P. B. Snyder, H. R. Wilson, J. R. Ferron, L. L. Lao, A. W. Leonard, T. H. Osborne, A. D. Turnbull, D. Mossessian, M. Murakami, and X. Q. Xu, Phys. Plasmas **9**, 2037 (2002).
- [15] T. E. Evans, R. A. Moyer, P. R. Thomas, J. G. Watkins, T. H. Osborne, J. A. Boedo, E. J. Doyle, M. E. Fenstermacher, K. H. Finken, R. J. Groebner, M. Groth, J. H. Harris, R. J. La Haye, C. J. Lasnier, S. Masuzaki, N. Ohya, D. G. Pretty, T. L. Rhodes, H. Reimerdes, D. L. Rudakov, M. J. Schaffer, G. Wang, and L. Zeng, Phys. Rev. Lett. **92**, 235003 (2004).
- [16] R. A. Moyer, T. E. Evans, T. H. Osborne, P. R. Thomas, M. Becoulet, J. Harris, K.-H. Finken, J. A. Boedo, E. J. Doyle, M. E. Fenstermacher, P. Gohil, R. J. Groebner, M. Groth, G. L.

- Jackson, R. J. La Haye, C. J. Lasnier, A. W. Leonard, G. R. McKee, H. Reimerdes, T. L. Rhodes, D. L. Rudakov, M. J. Schaffer, P. B. Snyder, M. R. Wade, G. Wang, J. G. Watkins, W. P. West, and L. Zeng
- [17] K. H. Burrell, T. E. Evans, E. J. Doyle, M. E. Fenstermacher, R. J. Groebner, A. W. Leonard, R. A. Moyer, T. H. Osborne, M. J. Schaffer, P. B. Snyder, P. R. Thomas, W. P. West, J. A. Boedo, A. M. Garofalo, P. Gohil, G. L. Jackson, R. J. La Haye, C. J. Lasnier, H. Reimerdes, T. L. Rhodes, J. T. Scoville, W. M. Solomon, D. M. Thomas, G. Wang, J. G. Watkins and L. Zeng, *Plasma Phys. Control. Fusion* **47**, B37 (2005).
- [18] T. E. Evans, R. A. Moyer, K. H. Burrell, M. E. Fenstermacher, I. Joseph, A. W. Leonard, T. H. Osborne, G. D. Porter, M. J. Schaffer, P. B. Snyder, P. R. Thomas, J. G. Watkins and W. P. West, *Nature Phys.* **2**, 419 (2006).
- [19] Y. Liang, H. R. Koslowski, P. R. Thomas, E. Nardon, B. Alper, P. Andrew, Y. Andrew, G. Arnoux, Y. Baranov, M. Becoulet, M. Beurskens, T. Biewer, M. Bigi, K. Crombe, E. De La Luna, P. de Vries, W. Fundamenski, S. Gerasimov, C. Giroud, M. P. Gryaznevich, N. Hawkes, S. Hotchin, D. Howell, S. Jachmich, V. Kiptily, L. Moreira, V. Parail, S. D. Pinches, E. Rachlew, and O. Zimmermann, *Phys. Rev. Lett.* **98**, 265004 (2007).
- [20] M. Bécoulet, E. Nardon, G. Huysmans, W. Zwingmann, P. Thomas, M. Lipa, R. Moyer, T. Evans, V. Chuyanov, Y. Gribov, A. Polevoi, G. Vayakis, G. Federici, G. Saibene, A. Portone, A. Loarte, C. Doeberl, C. Gimblett, J. Hastie and V. Parail, *Nucl. Fusion* **48**, 024003 (2008).
- [21] M. J. Schaffer, J. E. Menard, M. P. Aldan, J. M. Bialek, T. E. Evans and R. A. Moyer, *Nucl. Fusion* **48**, 024004 (2008).
- [22] I. Joseph, R. A. Moyer, T. E. Evans, M. J. Schaffer, A. M. Runov, R. Schneider, S. V. Kasilov, M. Groth, M.E. Fenstermacher, *J. Nucl. Mater.* **363-365**, 591 (2007).
- [23] I. Joseph, T. E. Evans, A. M. Runov, M. E. Fenstermacher, M. Groth, S. V. Kasilov, C. J. Lasnier, R. A. Moyer, G. D. Porter, M. J. Schaffer, R. Schneider and J. G. Watkins, *Nucl. Fusion* **48**, 045009 (2008).
- [24] M. F. Heyn, I. B. Ivanov, S. V. Kasilov, W. Kernbichler, I. Joseph, R. A. Moyer, and A. M. Runov, *Nucl. Fusion* **48**, 024005 (2008).
- [25] R. Fitzpatrick, *Phys. Plasmas* **5**, 3325 (1998).
- [26] A. Cole and R. Fitzpatrick, *Phys. Plasmas* **13**, 032503 (2006).
- [27] Jong-kyu Park, M. J. Schaffer, J. E. Menard, and A. H. Boozer, *Phys. Rev. Lett.* **99**, 195003

- (2007).
- [28] Jong-kyu Park, A. H. Boozer and J. Menard, Nucl. Fusion **48**, 045006 (2008).
 - [29] J.-K. Park, A. H. Boozer and J. E. Menard, Phys. Rev. Lett. **102**, 065002 (2009).
 - [30] A. H. Boozer and A. B. Rechester, Phys. Fluids **21**, 682 (1978).
 - [31] S.S. Abdullaev, K.H. Finken, M. Jakubowski and M. Lehnen, Nucl. Fusion **46**, S113 (2006).
 - [32] S. S. Abdullaev, M. Jakubowski, M. Lehnen, O. Schmitz, and B. Unterberg, Phys. Plasmas **15**, 042508 (2008).
 - [33] M. N. Rosenbluth, R. Z. Sagdeev, J. B. Taylor and G. M. Zaslavsky, Nucl. Fusion **6**, 297 (1966).
 - [34] A. B. Rechester and M. N. Rosenbluth, Phys. Rev. Lett. **40**, 38 (1978).

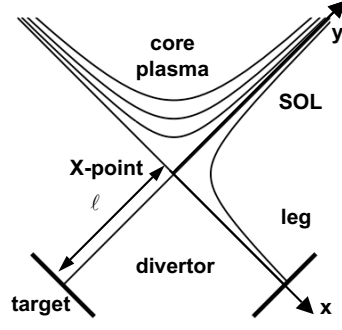


FIG. 1: The divertor region near the X-point: the x -axis lies along the outer divertor leg (lower separatrix branch) and the y -axis lies along the outer SOL (upper separatrix branch).

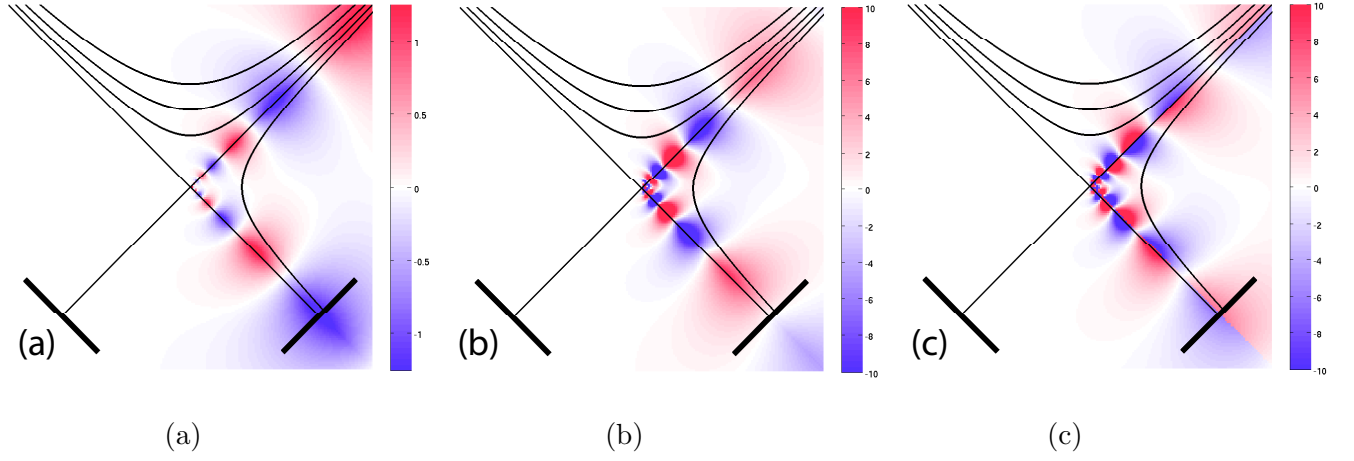


FIG. 2: (Color online) Perturbation fields far from the separatrix for a narrow current layer ($\tilde{B}_{leg} = \tilde{B}_{sol}$): (a) vector potential, (b) normal magnetic field, (c) tangential magnetic field. Parameters are $m_* = 4.5$, $\ell/\delta r = 25$; arbitrary units.

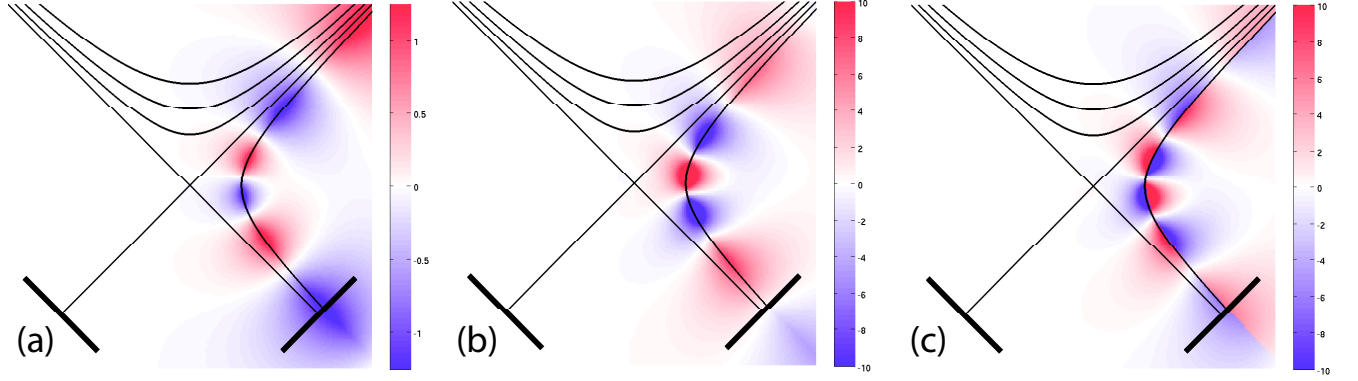


FIG. 3: (Color online) Perturbation fields close to the separatrix for a narrow SOL current density profile: (a) vector potential, (b) normal magnetic field, (c) tangential magnetic field. Parameters are $m_* = 4.5$, $\ell/\delta r = 25$; same color scale as Fig. 2.

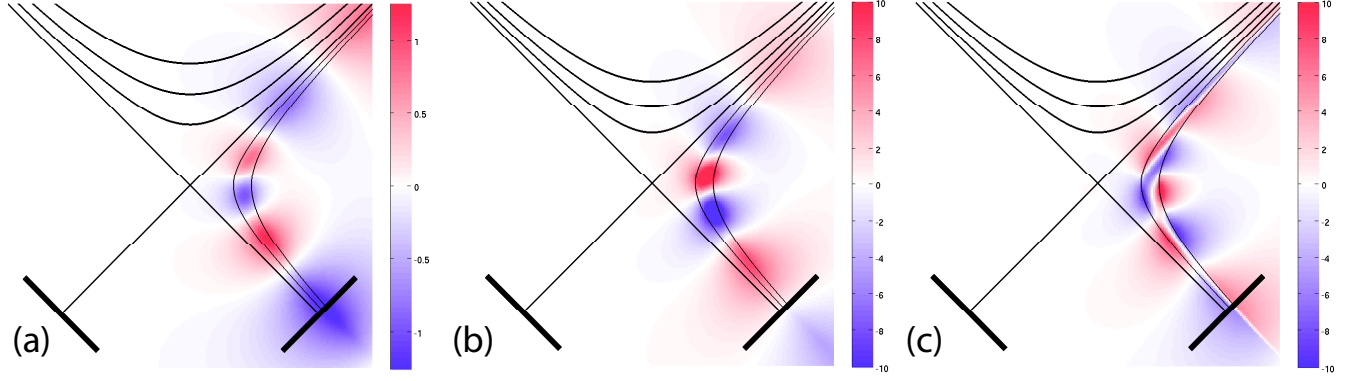


FIG. 4: (Color online) Perturbation fields close to the separatrix for a wide SOL current density profile for the case of a single coherence width: (a) vector potential, (b) normal magnetic field, (c) tangential magnetic field. Parameters are $m_* = 4.5$, $\ell/\delta r = 25$; same color scale as Fig. 2.

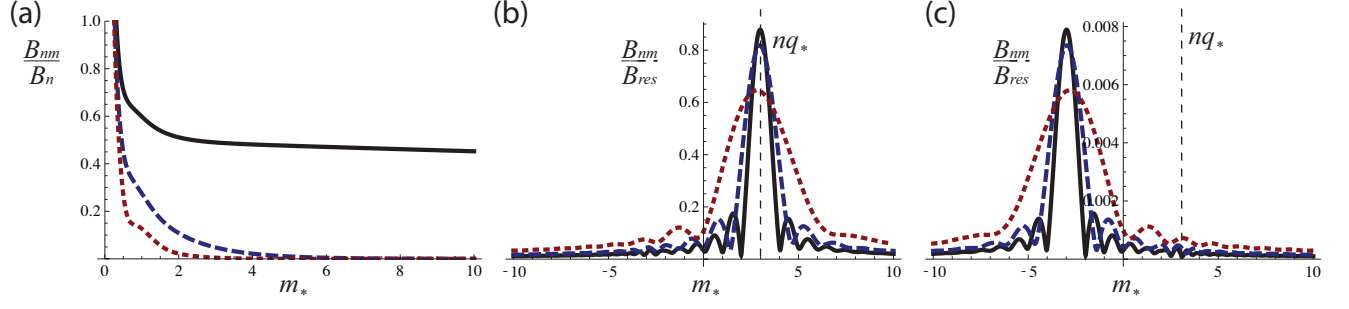


FIG. 5: (Color online) The flux surface averaged normal magnetic field perturbation spectrum \tilde{B}_{nm} versus m_* . (a) Near X-point current source normalized to $\tilde{B}_n = 2I_j/ca$ for $\psi = 10^{-2}$ and source locations $z_j = i$ (solid black), 0 (dashed blue), 1 (dotted red). (b) SOL surface current with $nq_* = 3$ on the separatrix (Eq. 48) normalized to \tilde{B}_{res} (Eq. 57) averaged over flux surfaces at $\rho/b = -10^{-1}, -10^{-2}, -10^{-3}$. (c) Divertor leg surface current on the separatrix (Eq. 54) for the same parameters.

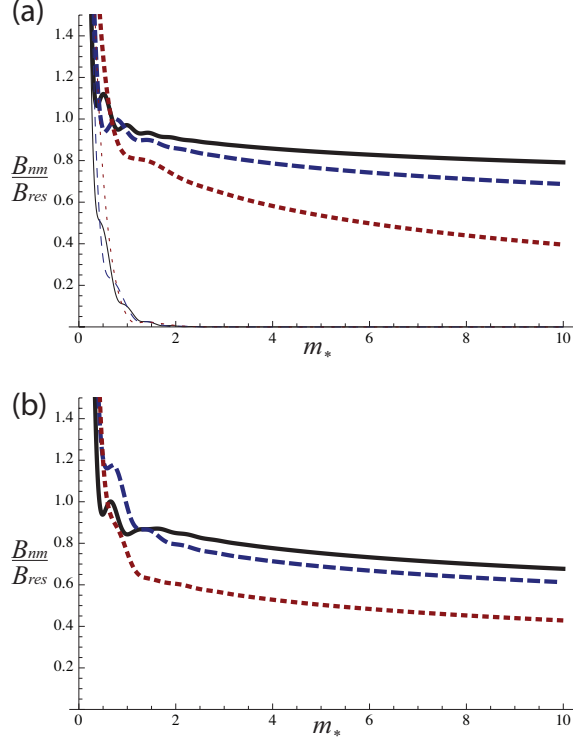


FIG. 6: (Color online) The flux surface averaged RMP spectrum $\tilde{B}_{n=qm}$ generated by the SOL and divertor current perturbations normalized to \tilde{B}_{res} (Eq. 57). (a) Analytic expressions for a current source on the separatrix $\delta\psi = 0$; SOL contribution (thick lines, Eq. 48) and divertor leg contribution (thin lines, Eq. 54); $\rho/b = 10^{-1}$ (solid black), 10^{-2} (dashed blue), 10^{-3} (dotted red). (b) The total numerically integrated resonant spectrum Eq. 47b for $\rho/b = 10^{-2}$ and $-\delta\psi/\psi = 0.1$ (solid black), 1 (dashed blue), 10 (dotted red).

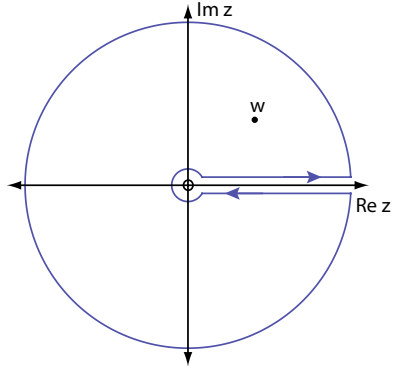


FIG. 7: The keyhole contour in the complex plane used to evaluate the integral in Eq. A1.